Chalcogenide Letters Vol. 22, No. 7, July 2025, p. 579 - 591

Study of the structural and elastic properties of nonlinear optical material $BaGa_4S_7$

H. J. Hou [a,*], J. X. Bian [a], K. J. Liu [b], W. X. Chen [a], X. W. Lu [a], S. R. Zhang [c]
[a] *School of Materials Engineering, Yancheng Institute of Technology, Yancheng 224051, China*
[b] *Shanghai PuChuang Intelligent Technology Co., Ltd, Shanghai 200120, China*
[c] *Department of Optoelectronics, Huaihua University, Huaihua 418000, China*

Utilizing first-principles method, the structural and anisotropic characteristics of $BaGa_4S_7$ has been meticulously investigated. The determined lattice parameters and elastic moduli exhibit a high degree of correlation with previously documented data. Based on its mechanical properties, $BaGa_4S_7$ demonstrates ductility and anisotropy. The anisotropic properties can be examined through a range of metrics.

(Received April 12, 2025; Accepted July 4, 2025)

Keywords: $BaGa_4S_7$, Structural, Mechanical

1. Introduction

Ternary chalcogenides are renowned for their pronounced physical and chemical attributes. These materials, lacking centrosymmetry, are particularly apt for deployment in the field of nonlinear optics (NLO) due to their unique optical properties [1]. A considerable level of enthusiasm has emerged for the utilization of contemporary coherent light emitting devices in a broad spectrum of applications, ranging from civil to defense-oriented technologies. These applications span multiple fields, including medicine (for noninvasive diagnostic procedures), telecommunications (enabling long-distance laser communications), information storage [2-5]. NLO materials an important role in facilitating frequency conversion through processes like frequency mixing, which involves methods such as second harmonic generation. These materials have demonstrated coherent laser emissions in spectral ranges that are difficult to attain using conventional laser methods. These regions encompass infrared (IR), far-infrared (FIR), and terahertz frequency ranges [6, 7]. For the Mid-IR spectrum, the majority of commercialized NLO materials consist of chalcopyrites such as $AgGaS_2$, $AgGaSe_2$ and $ZnGeP_2$ [8-11]. Within the category of nonlinear optical chalcogenide compounds that satisfy the previously noted exacting criteria, the $LiMQ_2$ series (where M denotes Al, Ga, or In, and Q corresponds to S, Se, or Te) is particularly distinguished [12-13]. Alternatively, substituting Ag with Li led to a substantial increase in the band gap [14]. Thus, $LiMQ_2$ crystals exhibit higher optical damage thresholds and broader infrared (IR) transparency compared to $AgGaQ_2$. However, compared to other stable materials, $LiMQ_2$ exhibits a relatively lower NLO coefficient [12-13]. Recent advancements have demonstrated BaM_4Q_7 (M = Ga or Al, and Q = S or Se) comprises several promising candidates

* Corresponding author: hhj@ycit.cn
https://doi.org/10.15251/CL.2025.227.579

for second-order NLO materials. These materials meet the specified criteria, including sufficient infrared (IR) optical transparency, a wide bandgap, and favorable second-order NLO coefficients. We focus on the specific materials from this family: $BaGa_4S_7$. In 1983, Eisenmann et al. were the first to synthesize the compounds $BaGa_4S_7$ and $BaAl_4S_7$[15]. Benghia has determined the physical characteristics of BaM_4S_7 (M = Ga or Al) [16]. Ginka Exner and colleagues present measurements of the physical properties for $BaGa_4S_7$ and $BaAl_4Se_7$[17]. Despite existing theoretical and experimental research on its associated characteristics, no theoretical studies have reported on how pressure influences its mechanical properties. The material's mechanical characteristics can offer a theoretical basis for its future processing.

2. Calculation details

To perform the required work, the Vienna Ab initio Simulation Package (VASP) was used for quantum mechanical modeling [18]. In the computational study, Projected Augmented Wave (PAW) potentials [19], are employed in tandem with the generalized gradient approximation (GGA) as formulated by Perdew et al, referred to as GGA-PBE [20]. In order to achieve the necessary convergence criteria for $BaGa_4S_7$, a Monkhorst-Pack grid of 7×7×6 *k*-points and a 500-eV energy cutoff for the plane waves are implemented, with a convergence threshold established at 10^{-5} eV.

3. Results and discussion

3.1. Structural characteristics of $BaGa_4S_7$

An extensive set of structural optimizations was performed by utilizing the DFT (GGA-PBE) approach to ensure accurate results. Table 1 compares the theoretical and experimental lattice parameters of $BaGa_4S_7$. The calculated lattice parameters exhibit a much closer agreement with experimental values, as compared to the GGA-PBE approach commonly used in other studies, which typically results in a 1-2% discrepancy [16, 21].

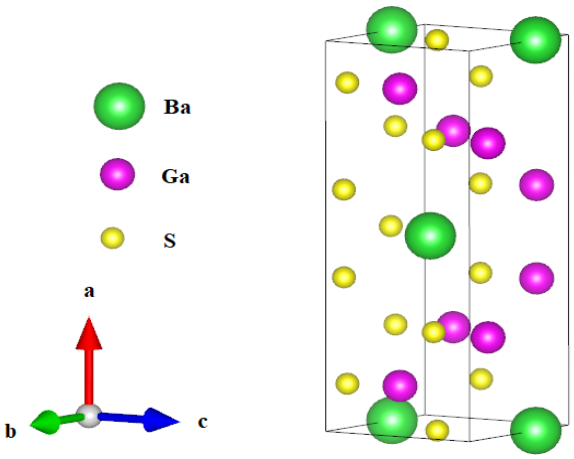

Fig. 1. Structural model of $BaGa_4S_7$.

Table 1. Experimental and theoretic structural properties of $BaGa_4S_7$.

Pressure (GPa)		a(Å)	b (Å)	c(Å)	ρ(g/cm^3)	V(Å^3)
This work	0	15.0799	6.3525	6.0400	3.6775	578.602
Ref.[16]	0	15.013	6.33	6.03		573.45
Ref.[16]	0	14.77	6.24	6.010		554.91
Exp.[21]	0	14.775	6.228	5.929		544.80
	5	14.4596	6.1156	5.7970	4.1508	512.624
	10	14.1387	5.9621	5.6441	4.4722	475.777
	15	13.9131	5.8420	5.5320	4.7322	449.643
	20	13.7401	5.7373	5.4443	4.9578	429.180

We place significant emphasis on the optimization of lattice parameters, as a well-optimized structure is crucial for obtaining accurate physical properties, including elastic properties.

3.2. Elastic properties

To evaluate the stability of $BaGa_4S_7$ and its anisotropic structural properties under pressure, we performed elasticity calculations on this compound. Specifically, computations were carried out to evaluate the effective elastic constants $\overline{C}_{ij}$. For the purpose of ascertaining the pressure-dependent elastic moduli of the orthorhombic phase of $BaGa_4S_7$, it is necessary to establish how these constants relate to those at ambient pressure [22].

$$\overline{C}_{\alpha\alpha} = C_{\alpha\alpha} - P\,, \quad \overline{C}_{\alpha\beta} = C_{\alpha\beta} + P(\alpha = 1,2...,6; \beta = 1,2...,6) \tag{1}$$

For orthorhombic systems, the criteria for mechanical stability necessitate that the calculated effective elastic constants must fulfill particular criteria.

$$\overline{C}_{11} > 0, \overline{C}_{44} > 0, \overline{C}_{55} > 0, \overline{C}_{66} > 0 \tag{2}$$

$$\overline{C}_{11}\overline{C}_{12} > \overline{C}_{22}{}^2 \tag{3}$$

$$\overline{C}_{11}\overline{C}_{22}\overline{C}_{33} + 2\overline{C}_{12}\overline{C}_{13}\overline{C}_{23} - \overline{C}_{11}\overline{C}_{23}{}^2 - \overline{C}_{22}\overline{C}_{13}{}^2 - \overline{C}_{33}\overline{C}_{12}{}^2 > 0 \tag{4}$$

Table 2. The elastic constants $\overline{C}_{ij}$ (GPa) of $BaGa_4S_7$.

Pressure(GPa)	C_{11}	C_{12}	C_{13}	C_{22}	C_{23}	C_{33}	C_{44}	C_{55}	C_{66}
0	47.7	14.9	12.2	57.9	8.54	58.8	15.2	12.8	12.6
Ref. [16]	71.62	27.66	22.53	76.22	16.42	73.09	18.12	22.88	25.98
Ref. [16]	76.98	35.83	26.86	94.94	21.79	78.98	20.87	28.20	23.97
5	91.5	38.1	25.3	94.8	21.7	100.2	20.6	22.1	21.4
10	124.3	53.2	35.6	118.8	30.1	131.9	23.9	28.0	27.4
15	152.6	66.4	45.8	138.9	37.6	160.9	26.2	32.9	32.6
20	177.9	79.1	56.0	156.8	44.5	187.7	27.5	38.1	38.2

The tabulated effective elastic constants in Table 2. The results converge with the observations documented in Reference [16]. Within 0 to 20 GPa, the orthorhombic phase of $BaGa_4S_7$ maintains its mechanical stable, as verified by meeting the established stability conditions. Subsequently, the Reuss-Voigt-Hill averaging technique was applied to obtain the bulk modulus (B), shear modulus (G), and Young's modulus (E) of $BaGa_4S_7$, as per references and presents in Table 3 [23-25]. The calculated E (40.2GPa) is marginally lower than the 80 GPa reported experimentally [17]. Poisson's ratio (v) functions as a key parameter for assessing the likelihood of a solid exhibiting brittle or ductile behavior. For $BaGa_4S_7$, the measured Poisson's ratio v maintains a value below 0.26 throughout the 0-20 GPa interval, indicative of its brittle nature. The B/G is another metric employed to gauge the degree of brittleness or ductility in solids [26]. The calculated B/G value for $BaGa_4S_7$ is below 1.75, signifying that the $BaGa_4S_7$ exhibits brittle characteristics. The values of v and the ratio B/G for BaGa4S7 are provided at different pressure (In Table 3). Additionally, the table illustrates the v and B/G for $BaGa_4S_7$, showing an increasing pattern as pressure rises. The results suggest that $BaGa_4S_7$ exhibits brittle behavior across the 0-20 GPa range.

Table 3. Elastic moduli (B, G, E), B/G, poisson's ratio v, wave velocities (v_l, v_t, v_m), and Debye temperature θ of $BaGa_4S_7$ at different pressures.

Pressure (GPa)	B (GPa)	G(GPa)	E (GPa)	B/G	v	v_l(km/s)	v_t(km/s)	v_m(km/s)	θ (K)
0	26.2	16.2	40.2	1.617	0.243	3.6053	2.0988	2.3284	239.9
Exp. [17]			80						
5	50.7	25.5	65.5	1.988	0.285	4.5173	2.4786	2.7632	296.4
10	68.0	31.8	82.6	2.138	0.298	4.9685	2.666	2.9776	327.4
15	83.4	37.0	96.7	2.254	0.307	5.2961	2.7962	3.1260	350.3
20	97.6	41.7	109.4	2.341	0.313	5.5588	2.9001	3.2448	369.3

Tabulated in Table 4 are the computed values for the anisotropic coefficients corresponding to shear deformations along distinct crystallographic axes (A_1, A_2, and A_3), the comprehensive anisotropic indicator (A^U), the bulk modulus (A_B) and shear modulus (A_G), the degree of anisotropy within the shear and bulk moduli (A_G and A_B), the directional-specific bulk

moduli (B_a, B_b, and B_c) associated with the *a*-, *b*-, and *c*-axes, respectively. The mechanical anisotropy indices can be evaluated using the following approaches [27-29]

$$A_1 = 4C_{44}/(C_{11} + C_{33} - 2C_{13}) \tag{5}$$

$$A_2 = 4C_{55}/(C_{22} + C_{33} - 2C_{23}) \tag{6}$$

$$A_3 = 4C_{66}/(C_{11} + C_{22} - 2C_{12}) \tag{7}$$

$$A^U = 5\frac{G_V}{G_R} + \frac{B_V}{B_R} - 6, \tag{8}$$

$$A_B = \frac{B_V - B_R}{B_V + B_R}, \tag{9}$$

$$A_G = \frac{G_V - G_R}{G_V + G_R} \tag{10}$$

$$B_a = a\frac{dP}{da} = \frac{\Lambda}{1 + \alpha + \beta} \tag{11}$$

$$B_b = b\frac{dP}{db} = \frac{B_\alpha}{\alpha} \tag{12}$$

$$B_c = c\frac{dP}{dc} = \frac{B_\alpha}{\beta} \tag{13}$$

where

$$\Lambda = C_{11} + 2C_{12}\alpha + C_{22}\alpha^2 + 2C_{13}\beta + C_{33}\beta^2 + 2C_{23}\alpha\beta$$

$$\alpha = \frac{(C_{11} - C_{12})(C_{33} - C_{13}) - (C_{23} - C_{13})(C_{11} - C_{13})}{(C_{33} - C_{13})(C_{22} - C_{12}) - (C_{13} - C_{23})(C_{12} - C_{23})}$$

$$\beta = \frac{(C_{22} - C_{12})(C_{11} - C_{13}) - (C_{11} - C_{12})(C_{23} - C_{12})}{(C_{22} - C_{12})(C_{33} - C_{13}) - (C_{12} - C_{23})(C_{13} - C_{23})}$$

Table 4 shows the computed values of A_1, A_2, and A_3, which demonstrate a divergence from the value of one. This indicates that $BaGa_4S_7$ exhibits a considerable degree of elastic anisotropy, with values as high as 20 GPa. At the same time, the *a*-axis exhibits the greatest value of directional-specific B_a, surpassing the values for the B_b and B_c. A vanishing A^U value signifies

the material's isotropic behavior. Deviations from zero imply a rise in anisotropic elastic responses. The indices A_B and A_G vary between 0 and 1, indicative of the degree of elastic anisotropy associated with bulk and shear properties, respectively. Table 4 details the pressure-dependent anisotropy indices. The anisotropic nature of $BaGa_4S_7$ is accentuated across the 0-20 GPa, culminating in elevated A^U values. The A^U for $BaGa_4S_7$ shows a progressive escalation up to 20 GPa.

Additionally, the material's hardness (H_V) and thermal conductivity (k) are computed through the application of specific mathematical expressions [30, 31]

$$H_V = 0.92(\frac{G}{B})^{1.137} G^{0.708} \tag{14}$$

$$\kappa_{\min} = 0.87 k_B M a^{-\frac{2}{3}} \rho^{\frac{1}{6}} E^{\frac{1}{2}} \tag{15}$$

Here, k_B stands for the Boltzmann constant, ρ signifies the material's density, and M_a is the mass per atom on average. At 0 GPa, the substance is characterized by a Vickers hardness value of 3.826 GPa and has a thermal conductivity of 0.4759 $W \cdot m^{-1} \cdot K^{-1}$. The results demonstrate that increased pressure leads to significant rises in both H_v and k values (As shown in Table 4).

Table 4. Our calculated elastic anisotropic indexes and factors (A_1, A_2, A_3, A^U, A_B, A_G, B_a, B_b and B_c), hardness H_V (GPa), and thermal conductivity k ($W.m^{-1}.K^{-1}$) of $BaGa_4S_7$ under pressures ranged from 0-20 GPa.

Pressure(GPa)	A_1	A_2	A_3	B_a	B_b	B_c	A^U	A_B	A_G	H_V	k
0	0.741	0.514	0.665	53.3	63.6	60.8	0.336	0.121	3.22	3.826	0.4759
Exp.[17]										6	
5	0.584	0.583	0.777	120.6	119.2	109.1	0.310	0.085	2.99	4.171	0.6199
10	0.517	0.588	0.802	178.9	151.0	148.4	0.368	0.113	3.53	4.490	0.7048
15	0.472	0.586	0.822	235.9	177.2	187.1	0.431	0.216	4.09	4.707	0.7698
20	0.434	0.596	0.866	293.9	200.5	224.3	0.497	0.343	4.67	4.908	0.8252

By leveraging elastic constants as input parameters, the Debye temperature can be ascertained in the low-temperature regime utilizing established correlations [32]

$$\theta = \frac{h}{k_B}[\frac{3n}{4\pi}(\frac{NA\rho}{M})]^{1/3} v_m \tag{16}$$

The computation of mean sound speed employs a set of constants: the Planck constant ($\hbar$), Boltzmann's constant (k), and Avogadro's number (N_A). Additionally, it incorporates variables like the atomicity of the formula unit (n), molar mass of the formula unit (M), material density (ρ), and mean velocity of sound (v_m)[33]

$$v_m = [\frac{1}{3}(\frac{2}{v_t^3} + \frac{1}{v_l^3})]^{-1/3} \quad (17)$$

The determination of the velocities for longitudinal and transverse elastic waves is based on a specific relationship, in which v_l stands for the speed of the longitudinal wave, while v_t signifies the speed of the transverse wave[34, 35]

$$v_t = (\frac{G}{\rho})^{1/2} \quad (18)$$

$$v_l = [(B + \frac{4G}{3}) / \rho]^{1/2} \quad (19)$$

Tabulated data in Table 3 delineates the longitudinal, transverse, and mean sound speeds, in conjunction with the Debye temperature for $BaGa_4S_7$ subjected to a range of pressures. Examination of the data presented in Table 3 indicates a positive correlation; as pressure intensifies, there is a corresponding escalation in the propagation speeds of longitudinal, shear, and average sound waves, alongside an uplift in the Debye characteristic temperature.

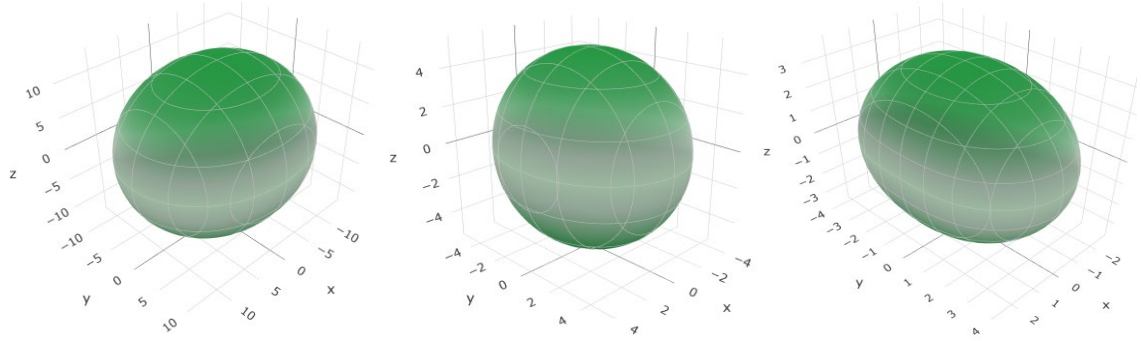

(0GPa) **(10GPa)** **(20GPa)**

Fig. 5. The 3D surface constructions of β (TPa^{-1}) of $BaGa_4S_7$.

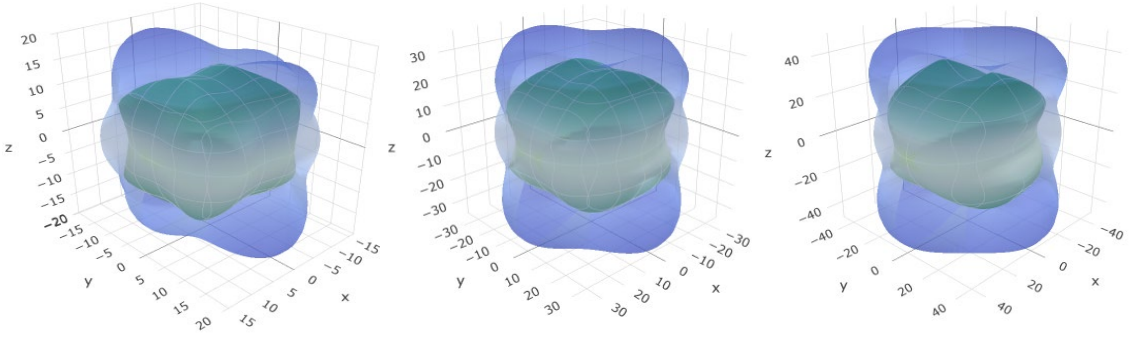

(0GPa) **(10GPa)** **(20GPa)**

Fig. 6. The 3D surface constructions of G (GPa) of $BaGa_4S_7$.

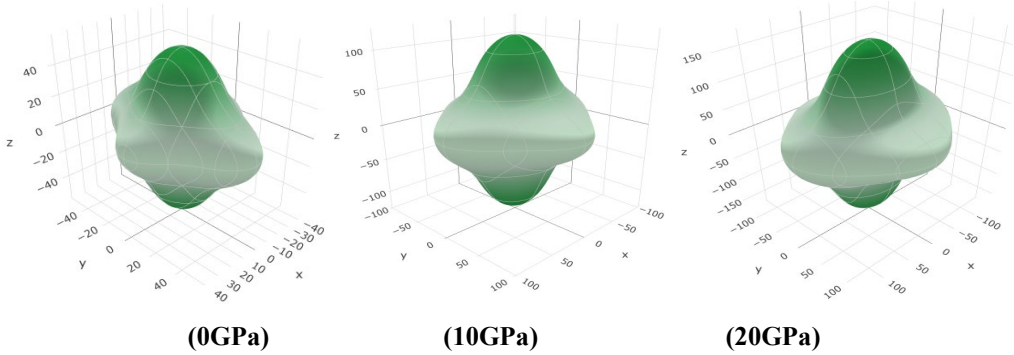

Fig. 7. The 3D surface constructions of E (GPa) of $BaGa_4S_7$.

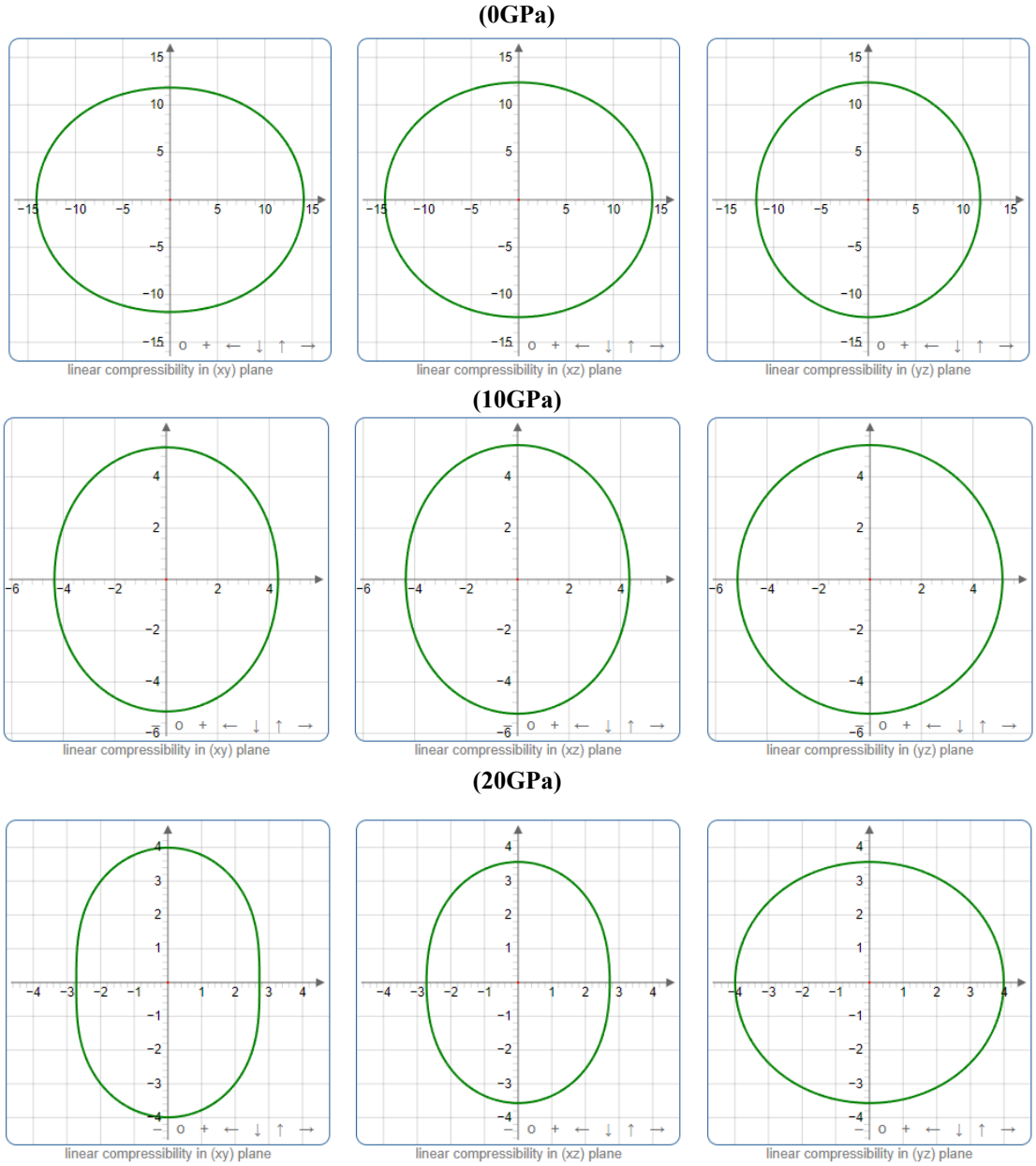

Fig. 8 Projections of β (TPa^{-1}) of $BaGa_4S_7$.

(0GPa)

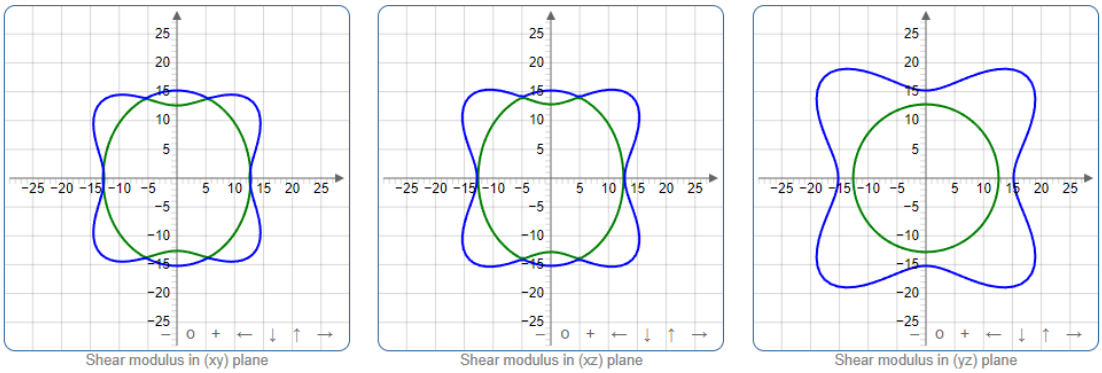

(10GPa)

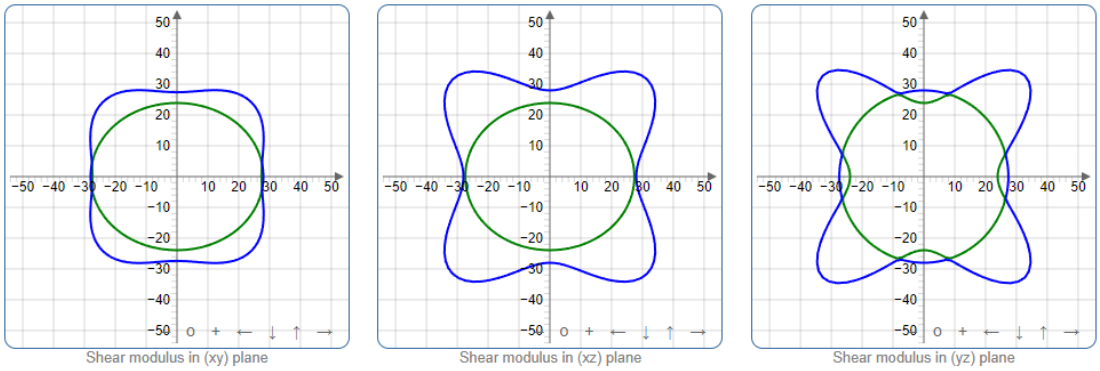

(20GPa)

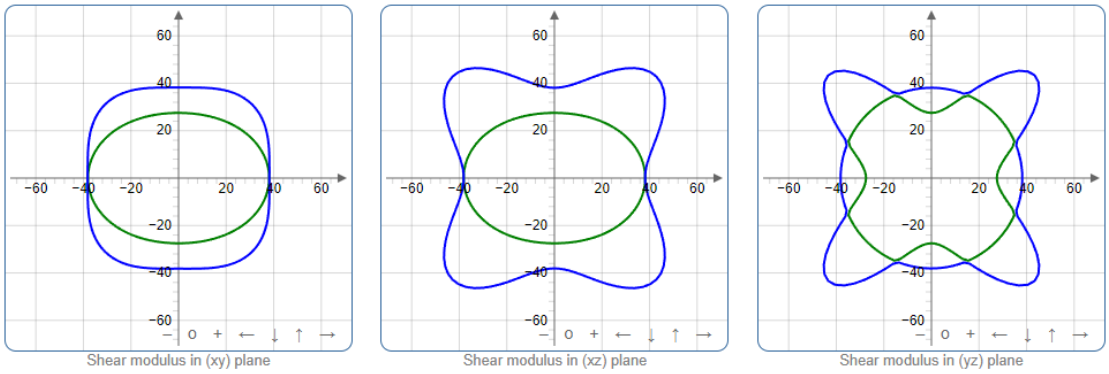

Fig. 9. Projections of G (GPa) of $BaGa_4S_7$.

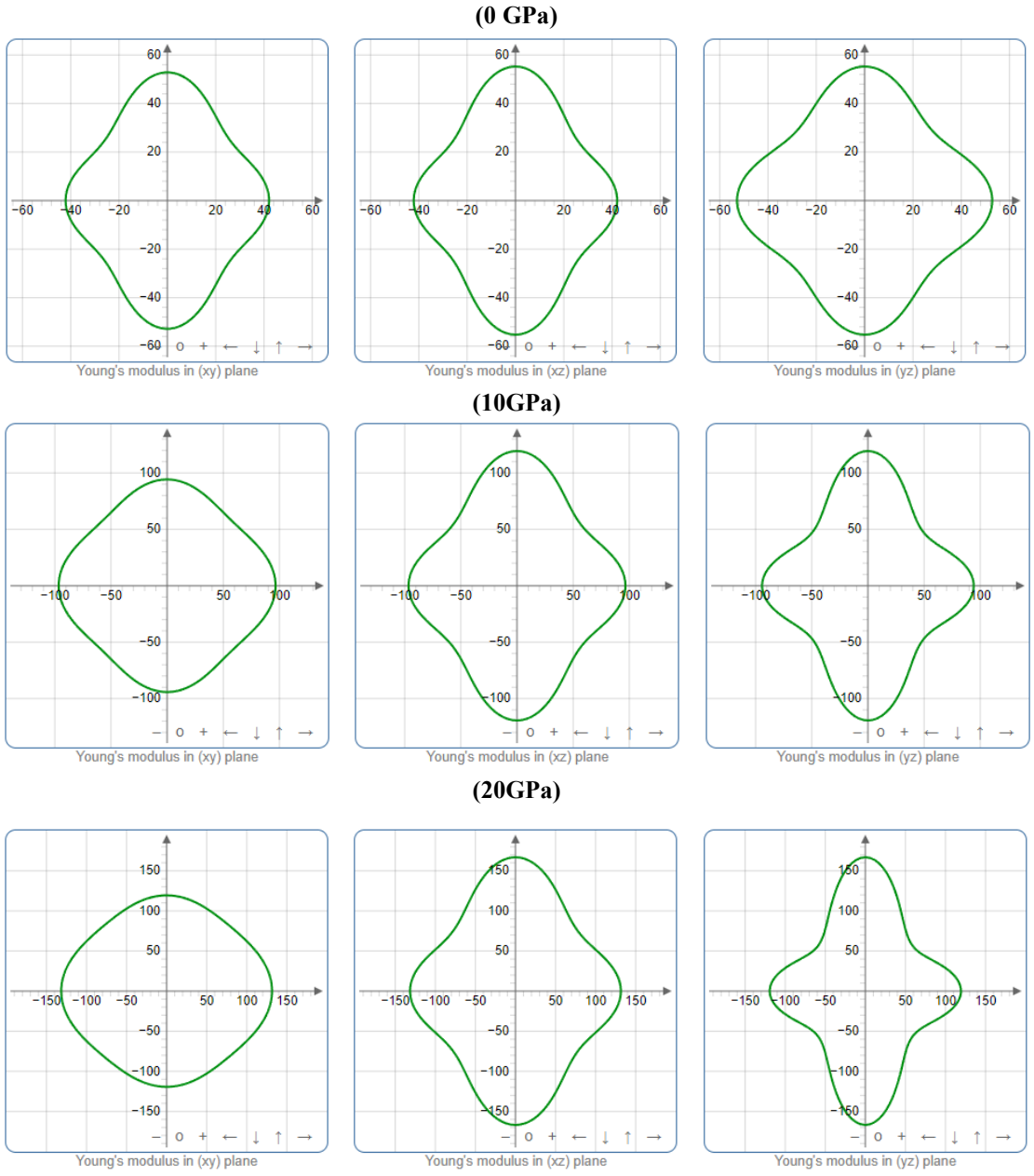

Fig. 10. Projections of E (GPa) of $BaGa_4S_7$.

To thoroughly examine the mechanical anisotropy, this investigation probed the variations in linear compressibility (β), shear modulus (G), and Young's modulus (E) for $BaGa_4S_7$[36]. Figs.5-7 depict the interrelationship of β, G, and E within the structure of $BaGa_4S_7$. In structures that exhibit isotropy, spatial correlations appear in a spherical arrangement. Deviations from this spherical form can be used as indicators to identify anisotropic characteristics. The pressure-dependent, non-uniform spatial profile of β, G, and E within $BaGa_4S_7$ suggests a pronounced level of directional dependence in its material characteristics. In order to assemble a more extensive body of data on the pressure-dependent anisotropic behavior of $BaGa_4S_7$'s β, G,

and E, Figs. 8- 10 illustrate the planar projections of these properties in the different planes, respectively. In substances exhibiting isotropic characteristics, the projection curve assumes a spherical form. However, in the xy and xz planes, a marked enhancement in the discrepancy of β, G, and E is observed. Concurrently, the anisotropic elasticity of $BaGa_4S_7$ was comprehensively analyzed under various pressure using the ratios of β_{max}/β_{min}, G_{max}/G_{min}, and E_{max}/E_{min}. A higher degree of linear compressional anisotropy can be deduced from a larger β_{max}/β_{min}, along with the corresponding G_{max}/G_{min} and E_{max}/E_{min}. The β_{max}/β_{min} ratios at different pressures are as follows: 1.1942 at 0 GPa, 1.1054 at 5 GPa, 1.2053 at 10 GPa, 1.3316 at 15 GPa, and 1.4655 at 20 GPa. The G_{max}/G_{min} ratios are observed to be 1.973 at 0 GPa, dropping slightly to 1.805 at 5 GPa, before rising to 1.939 at 10 GPa, 2.034 at 15 GPa, and 2.203 at 20 GPa. Furthermore, the E_{max}/E_{min} ratios are recorded as 1.628 at 0 GPa, gradually increasing to 1.635 at 5 GPa, 1.748 at 10 GPa, 1.891 at 15 GPa, and 2.048 at 20 GPa. Based on the provided data, it is clear that anisotropy diminishes as pressure increases within the 0-20 GPa.

4. Conclusions

This research employed a first-principles computational method to analyze the structural and elastic attributes of the orthorhombic variant of $BaGa_4S_7$. The calculated elastic properties demonstrate that $BaGa_4S_7$ is mechanically stable, meeting the established stability criteria. Moreover, the determined v and B/G imply a proclivity towards brittleness in $BaGa_4S_7$. The material's compressibility is found to be more pronounced along the a- and c-axis directions, with a relative decrease in compressibility observed along the b-axis direction. The elastic characteristics of $BaGa_4S_7$ demonstrate a clear anisotropic pattern.

References

[1] I. Chung, M.G. Kanatzidis, Chem. Mater. 26, 849(2014); https://doi.org/10.1021/cm401737s

[2] D.N. Nikogosyan (Ed.), Nonlinear Optical Crystals: A Complete Survey, Springer Science & Business Media, 2006.

[3] C. Gmachl, F. Capasso, R. Kohler, A. Tredicucci, A.L. Hutchinson, D.L. Sivco, J.N. Baillargeon, A.Y. Cho, IEEE Circ. Dev. Mag. 16, 10 (2000); https://doi.org/10.1109/101.845908

[4] T.K. Bera, J.I. Jang, J.-H. Song, C.D. Malliakas, A.J. Freeman, J.B. Ketterson, M.G. Kanatzidis, J. Am. Chem. Soc. 132, 3484(2010); https://doi.org/10.1021/ja9094846

[5] F.K. Tittel, D. Richter, A. Fried, Solid-State Mid-Infrared Laser Sources, Springer, 2003, 458-529; https://doi.org/10.1007/3-540-36491-9_11

[6] N. Bloembergen (Ed.), Nonlinear Optics, World Scientific, 1996; https://doi.org/10.1142/9789814261081

[7] P.S. Halasyamani, K.R. Poeppelmeier, Noncentrosymmetric Oxides Chem. Mater. 10, 2753(1998); https://doi.org/10.1021/cm980140w

[8] Peter G Schunemann, Scott D Setzler, J. Cryst. Growth 211, 257(2000); https://doi.org/10.1016/S0022-0248(99)00855-6

[9] J. Cheng, S.F. Zhu, B.J. Zhao, B.J. Chen, Z.Y. He, Q. Fan, T. Xu, J. Cryst. Growth 318, 729 (2011); https://doi.org/10.1016/j.jcrysgro.2010.11.008

[10] B.J. Chen, S.F. Zhu, B.J. Zhao, J.J. Zhang, Y. Huang, M. Li, J. Liu, B. Tan, R.L. Wang, Z.Y. He, J. Cryst. Growth 292, 490 (2006); https://doi.org/10.1016/j.jcrysgro.2006.04.057

[11] G. Anandha Babu, R. Subramaniyan Raja, N. Karunagaran, R. Perumal Ramasamy, P. Ramasamy, S. Ganesamoorthy, P.K. Gupta, J. Cryst. Growth 338, 42 (2012); https://doi.org/10.1016/j.jcrysgro.2011.10.039

[12] L. Isaenko, I. Vasilyeva, A. Merkulov, A. Yelisseyev, S. Lobanov, J. Cryst. Growth 275, 217 (2005); https://doi.org/10.1016/j.jcrysgro.2004.10.089

[13] L. Isaenko, A. Yelisseyev, S. Lobanov, P. Krinitsin, V. Petrov, J.-J. Zondy, J. Non Cryst. Solids 352, 2439 (2006); https://doi.org/10.1016/j.jnoncrysol.2006.03.045

[14] L. Bai, Z. Lin, Z. Wang, C. Chen, M.-H. Lee, J. Chem. Phys. 120, 8772 (2004); https://doi.org/10.1063/1.1687338

[15] B. Eisenmann, M. Jakowski, H. Schafer, Rev. Chim. Miner. 20, 329 (1983)

[16] Ali Benghia, Tahar Dahame, Bachir Bentria, Opt. Mater. 54, 269 (2016); https://doi.org/10.1016/j.optmat.2016.02.027

[17] Ginka Exner, Aleksandar Grigorov, Valeriy Badikov, Valentin Petrov, Opt. Mater. 133, 112994 (2022); https://doi.org/10.1016/j.optmat.2022.112994

[18] G. Kresse, J. Furthmüller, Phys. Rev. B 54, 11169 (1996); https://doi.org/10.1103/PhysRevB.54.11169

[19] G. Kresse, D. Joubert, Phys. Rev. B 59, 1758(1999); https://doi.org/10.1103/PhysRevB.59.1758

[20] J. P. Perdew, K. Burke, M. Ernzerhof, Phys. Rev. Lett. 77, 3865 (1996); https://doi.org/10.1103/PhysRevLett.77.3865

[21] J.A.R. Stiles, M. Kamkar, Barium thioaluminate phosphor materials with novel crystal structures, Google Patents, 2008.

[22] F. Mouhat, F. X. Coudert, Physical Review B. 90 (22), 224104(2014); https://doi.org/10.1103/PhysRevB.90.224104

[23] W. Voigt, Handbook of Crystal Physics, Taubner, Leipzig, 1928.

[24] A. Reuss, Z. Angew, Math. Mech. 9, 49 (1929); https://doi.org/10.1002/zamm.19290090104

[25] R. Hill, Proc. Phys. Soc. A 65, 349 (1952); https://doi.org/10.1088/0370-1298/65/5/307

[26] S. F. Pugh, Philos. Mag. 45, 823(1954); https://doi.org/10.1080/14786440808520496

[27] S. I. Ranganathan, M. Ostoja-Starzewski, Phys. Rev. Lett. 101, 055504 (2008); https://doi.org/10.1103/PhysRevLett.101.055504

[28] D. H. Chung, W. R. Buessem, in: F.W. Vahldiek, S.A. Mersol (Eds.) Anisotropy in Single Crystal Refractory Compound, Plenum, New York, 1968.

[29] P. Ravindran, L. Fast, P. A. Korzhavyi, B. Johansson, J. Appl. Phys. 84, 4891(1998); https://doi.org/10.1063/1.368733

[30] J. Feng, B. Xiao, J. Chen, Y. Du, J. Yu, R. Zhou, Mater. Des. 32, 3231 (2011); https://doi.org/10.1016/j.matdes.2011.02.043

[31] O. Anderson, J. Phys. Chem. Solids 24, 909(1963);

https://doi.org/10.1016/0022-3697(63)90067-2

[32] F. Arab, F.A. Sahraoui, K. Haddadi, A. Bouhemadou, L. Louail, Phase Transitions 89, 480(2016); https://doi.org/10.1080/01411594.2015.1089574

[33] S. Chen, Y. Sun, Y.H. Duan, B. Huang, M.J. Peng, J. Alloys Compd. 630, 202(2015); https://doi.org/10.1016/j.jallcom.2015.01.038

[34] W. Kim, J. Mater Chem C 3, 10336(2015); https://doi.org/10.1039/C5TC01670C

[35] J. Yang, M. Shahid, C.L. Wan, J. Feng, W. Pan, J. Eur. Ceram. Soc. 37, 689(2017); https://doi.org/10.1016/j.jeurceramsoc.2016.08.034

[36] R. Gaillac, P. Pullumbi, F-X. Coudert, J Phys: Condens Matter 28, 275201(2016); https://doi.org/10.1088/0953-8984/28/27/275201